Monostatic Multi-Target Wi-Fi-Based Breathing Rate Sensing Using openwifi

Andreas Toftegaard Kristensen*, Sitian Li*, Alexios Balatsoukas-Stimming†, and Andreas Burg*
*Telecommunication Circuits Laboratory, École polytechnique fédérale de Lausanne, Switzerland
†Eindhoven University of Technology, The Netherlands

2024 IEEE Wireless Communications and Networking Conference (WCNC) | 979-8-3503-0358-2/24/$31.00 ©2024 IEEE | DOI: 10.1109/WCNC57260.2024.10570912

***Abstract*—Continuous monitoring of human activity and vital signs has become increasingly important in healthcare and consumer applications. While wearables and others sensors are already in widespread use, they often suffer from issues such as discomfort and the need for physical contact. To address these limitations, wireless sensing using radio signals has emerged as a promising alternative. However, most previous work has focused on bistatic setups utilizing commodity Wi-Fi devices. In this work, we use the open-source openwifi platform for monostatic multi-antenna Wi-Fi sensing for contactless breathing rate measurements. We also present a method for simultaneous estimation of the breathing rate of two targets. Experimental results using CNC machines for emulating human breathing demonstrate the effectiveness of our method and setup for targets at a few meters distance. Even in challenging scenarios where the breathing rates are similar, the targets are close together, and the targets have the same angle of arrival, we achieve an average error of 0.61 breaths per minute. We further validate our setup and method by collecting human breathing data from two subjects, which can clearly be distinguished using our setup and method. Moreover, our results indicate that self-interference cancellation is not necessary for close-range breathing rate sensing.**

***Index Terms*—ISAC, device-free sensing, RF sensing, monostatic sensing, Wi-Fi sensing, openwifi**

I. Introduction

Over the last few decades, there has been a growing demand from consumers and healthcare providers for continuous monitoring of human activity and physiology [1]. Various methods are currently used for monitoring physical activity and vital signs, such as self-reported measures [2] and objective measures using wearable devices and other sensors [3].

Among the key indicators of health are the four vital signs: body temperature, blood pressure, pulse, and breathing rate [4]. Wearables such as smartwatches, chest bands, and smart patches can capture these and other metrics such as glucose levels and step counts, which are essential for healthcare analytics [1]. However, many devices are also burdened by challenges such as the need to actually wear these devices and significant discomfort associated with sensors that are tightly attached to the body. Such physical constraints can be a hurdle for many individuals, particularly the elderly who may require assistance. Wearable devices also typically have gaps in their measurement data during charging periods, for example over night. In an ideal scenario, a monitoring system would enable contactless, uninterrupted, effortless data collection, requiring minimal input or adaptation from the user.

Wireless sensing based on radio signals for non-invasive and contact-free sensing has gained traction as a promising alternative to traditional monitoring methods [5] and has already been used for many applications such as detecting falls [6], human activity [7], and vital signs [8]. Initial wireless sensing strategies opportunistically extracted channel state information (CSI) from readily available consumer devices, such as standard Wi-Fi routers [9, 10, 11, 12, 13, 14], thus avoiding the need for specialized hardware. In contrast to these opportunistic wireless sensing strategies, integrated sensing and communication (ISAC) significantly refines the joint sensing and communication approach. In an ISAC system, the same hardware and frequency band can be used for both tasks in parallel enabling joint optimization. As such, ISAC has been identified as a crucial technique in various areas, including vehicular networks, smart cities, and remote sensing [15].

ISAC can be implemented in one of two fundamental physical configurations: monostatic using a single transceiver or bistatic using spatially and physically separated transmitter and receiver. An important issue for bistatic setups is the unsynchronized transmitter and receiver clocks, which causes imperfections such as carrier frequency offset (CFO), sampling frequency offset (SFO), and sampling time offset (STO) that severely impair the sensing performance. While these imperfections can be mitigated by calibration methods such as taking the ratio of subcarriers between different receive antennas [16], any calibration implies a loss of information and additional noise. Monostatic setups use a shared clock and thus eliminate these imperfections. However, they face unique challenges like strong self-interference, that may require cancellation strategies similar to those used in full-duplex radio [17]. Despite these hurdles, monostatic setups offer several advantages beyond just eliminating imperfections, such as increased security through authorized sensing methods like local CSI fuzzing [18].

Numerous tools exist for Wi-Fi based sensing, such as the Intel Wi-Fi Link 5300 for 802.11n [9], Atheros CSI [10], Wi-ESP [12], Nexmon CSI for 802.11ac [11], PicoScenes [13], and AX-CSI for 802.11ax [14]. Despite their advantages, these tools often use commodity Wi-Fi devices with non-modifiable hardware and control over settings such as automatic gain

979-8-3503-0358-2/24/$31.00 ©2024 IEEE

control (AGC) and additional data like raw in-phase and quadrature (I/Q) samples are often unavailable. Control over AGC settings can be essential for sensing, as AGC fluctuations between packets can significantly affect the received signal, overshadowing effects from sensing targets. Access to raw I/Q samples can also enhance sensing sensitivity by providing extra data for channel estimation beyond training fields. Finally, such systems cannot operate in a monostatic setting with concurrently activated and synchronized transmitter and receiver and therefore require complex and sensitive calibration.

Contributions: In this work, we use an open-source[1] testbed for monostatic multi-antenna Wi-Fi sensing based on openwifi [19]. Moreover, we describe a method for simultaneous estimation of the breathing rate of two targets. The experimental results from our testbed show that this method works well even when the breathing rates are close in frequency, when the targets are at the same angle of arrival (AoA), and when the targets are close to each other. Moreover, the results show that, in our setup, self-interference cancellation is not necessary for close-range (few meters) breathing rate sensing.

II. Background

In this section, we introduce some background on the 802.11n standard and on breathing rate estimation using CSI.

A. Channel State Information (CSI)

In an 802.11n system, the transmitter sends a frame of several orthogonal frequency-division multiplexing (OFDM) symbols. Some of these symbols contain known data for estimating the wireless channel. The receiver initially synchronizes to a preamble at the start of the Wi-Fi frame. Once synchronized, the frequency response of the channel (generally referred to as CSI) is obtained. This CSI is characterized and affected by changes in the attenuation and delay of the multipath components of the wireless channel as described by

$$H_l(k,\tau) = \sum_{p=1}^{P} \alpha_{p,l} e^{-j2\pi(k\Delta f - f_c)\tau_{p,l}}, \quad (1)$$

where P is the number of paths, $\alpha_{p,l}$ and $\tau_{p,l}$ are the attenuation and delay of path p for Wi-Fi frame l, k is the subcarrier index, Δf is the subcarrier spacing, and f_c is the carrier frequency.

B. Breathing Estimation with CSI

Multipath components reflected from the human chest lead to periodic changes to $\alpha_{p,l}$ and $\tau_{p,l}$, which are captured the CSI. In particular, a change in the delay (due to chest movements) is directly reflected in the phase of the contribution of this path to the CSI. Nevertheless, the impact on the sum of the many paths is typically small and does not result in a corresponding phase shift that could be observed directly.

In most Wi-Fi sensing research, a subset of CSI subcarriers is selected as the main feature for sensing. These subcarriers are often selected based on statistical measures such as high mean absolute deviations or variances [20, 21]. In contrast, the authors of [16, 22] employ the breathing-to-noise ratio (BNR) method, which involves calculating the power spectral density (PSD) of each subcarrier and selecting those with the highest power in the range of human breathing, which is generally 12 to 15 breaths per minute (bpm) at rest [23, p. 588]. Alternatively, by transforming the CSI into a channel impulse response (CIR) with an inverse Fourier transform on the CSI, the multipath information can be used to more easily select the delay bins that best capture the relevant paths [24]. Then, breathing rate estimation can be done by calculating the PSD of only the relevant paths over time.

However, when there are multiple people present, breathing rate estimation becomes much more challenging and additional methods generally have to be applied. In [22], the authors introduced MultiSense, which applies independent component analysis (ICA) to successfully recover individual respiration patterns for up to five individuals. Several works also apply Root-MUSIC for extracting multiple respiration rates [25, 20].

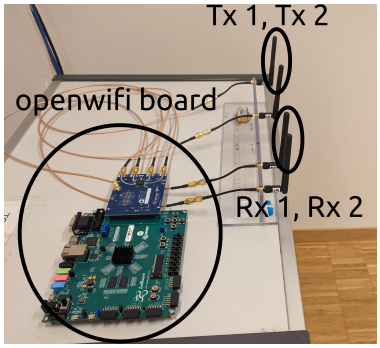

Fig. 1: ZedBoard with Tx and Rx antenna connected.

III. Testbed and Breathing Rate Estimation Algorithm

In this section, we describe the hardware and software of the monostatic open-source testbed used to obtain the CSI and our proposed algorithm for multi-target breathing rate sensing.

A. Hardware

For the implementation of our testbed, we used a ZedBoard field-programmable gate array (FPGA) development kit with the AD-FMCOMMS2-EBZ radio frequency (RF) front-end which has 4 RF chains for supporting two receive (Rx) and two transmit (Tx) antennas [26]. The setup is shown in Fig. 1. The FPGA board runs openwifi, which is an open-source software-defined radio (SDR) implementation of the IEEE 802.11 Wi-Fi standard [19] including the physical (PHY) layer and the lower medium-access control (MAC) layer of 802.11n on the FPGA. The programmable hardware allows for extracting raw I/Q baseband samples in addition to the CSI from the PHY layer channel estimation. The board can be configured to

[1] github.com/A-T-Kristensen/wcnc2024_monostatic_sensing_openwifi

transmit and receive simultaneously, thus enabling full-duplex monostatic sensing. A common clock signal is used for the transmitter and the receiver, which eliminates CFO, SFO, and STO impairments. Operating as a fully functional 802.11n device, openwifi supports Ad-hoc, Station, AP, and Monitor modes, offering versatility for many research scenarios.

B. Collecting and Processing I/Q samples

For our monostatic setup, we generate data on the openwifi board and receive the transmitted signal. We use a packet injection application running in Linux to generate the transmitted data. The collection of I/Q samples on the receiver side is triggered when the first I/Q sample is transmitted from the FPGA. The raw I/Q samples are then sent to a host computer. The stored samples are then imported for processing using the MATLAB WLAN toolbox. In particular, we perform synchronization to the legacy short training field (L-LTF) and legacy long training field (L-LTF) fields to then extract the L-LTF and high throughput long training field (HT-LTF) symbols and then calculate the CSI.

C. Multi-Target Breathing Rate Estimation

For breathing-rate estimation, we use the CIR to more easily remove irrelevant paths and the associated noise, based on the size of the room and the limited bandwidth of the Wi-Fi signal. Specifically, we use only the first two delay bins of the CIR for each receive antenna. The concatenated CIR snippets at time l are denoted by a vector $\mathbf{h}_l \in \mathbb{C}^D$ with $D = 4$ entries (two bins and two antennas). A sequence of $\mathbf{h}_l$ obtained from multiple Wi-Fi frames is denoted by a feature matrix $\mathbf{H} \in \mathbb{C}^{T\times D}$, where each row represents one $\mathbf{h}_l$ at a given time instance. In the work of [27], we introduced a CIR combination method that does not require prior knowledge of the position of the target. This method combines different delay bins in the CIR by solving a generalized eigenvalue problem such that the power in the combined vector in the band-of-interest (BoI) is maximized according to

$$\arg\max_{\mathbf{w}} \quad \mathbf{w}^H\mathbf{A}\mathbf{w}\,, \tag{2}$$

$$\text{s.t.} \quad \mathbf{w}^H\mathbf{B}\mathbf{w} = 1\,, \tag{3}$$

where $\mathbf{A} = \mathbf{H}^H\mathbf{F}_I^H\mathbf{F}_I\mathbf{H}$ is the power in the BoI, $\mathbf{B} = \mathbf{H}^H\mathbf{F}^H\mathbf{F}\mathbf{H}$ is the power in the full spectrum, $\mathbf{F}$ is the discrete Fourier transform (DFT) matrix, and $\mathbf{F}_I$ denotes rows in the DFT matrix corresponding to the frequencies in the BoI. The normalized optimal solution $\frac{\mathbf{w}^*}{\|\mathbf{w}^*\|}$ is an eigenvector of the generalized eigenvalue problem with matrices $\mathbf{A}$ and $\mathbf{B}$ [28], denoted by $(\mathbf{A}, \mathbf{B})$. We obtain the eigenvectors $\tilde{\mathbf{w}}_i$ from the eigenvalue decomposition of $(\mathbf{A}, \mathbf{B})$. Afterwards, each $\tilde{\mathbf{w}}_i$ is scaled to obtain one candidate $\mathbf{w}_i$ for the optimal solution

$$\mathbf{w}_i = \left(\tilde{\mathbf{w}}_i^H\mathbf{B}\tilde{\mathbf{w}}_i\right)^{-\frac{1}{2}}\tilde{\mathbf{w}}_i\,. \tag{4}$$

Finally, we select the $\mathbf{w}_i$ that leads to the largest $\mathbf{w}_i^H\mathbf{A}\mathbf{w}_i$ as the optimal solution $\mathbf{w}^* = \mathbf{w}_{i_{\max}}$.

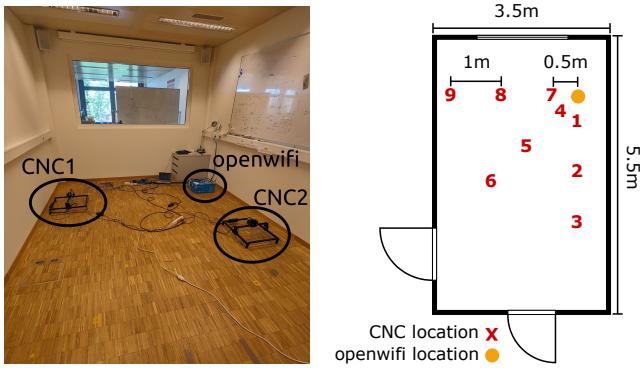

Fig. 2: Photo and floorplan of the experimental setup.

Based on this BoI fusion method, we propose a novel three-step *estimate-focus-delete* method to successively estimate the breathing rate for multiple targets as follows:

1) Estimate: First, we average over the rows of $\mathbf{H}$ and calculate the PSD. Then, we define the frequency in the PSD with the maximum amplitude as the BoI and use the CIR combination method from [27] described earlier in this subsection to get the combined feature vector $\widehat{\mathbf{h}} = \mathbf{H}\mathbf{w}_{i_{\max}}$.

2) Focus: The strongest frequency component is then estimated from $\widehat{\mathbf{h}}$ and selected as the new BoI for the estimate step. The estimate and focus steps are repeated until the BoI converges, which typically takes one or two iterations.

3) Delete: Once the BoI has converged, the BoI is used as the estimated breathing rate of the current target. We then calculate the residual feature matrix $\widehat{\mathbf{H}}_{\text{res}} = \mathbf{H}\mathbf{V}_{\text{res}} \in \mathbb{C}^{T\times(D-1)}$ from $\mathbf{H}$ using the matrix $\mathbf{V}_{\text{res}} = \begin{bmatrix}\tilde{\mathbf{w}}_1 & \cdots & \tilde{\mathbf{w}}_{i_{\max}-1} & \tilde{\mathbf{w}}_{i_{\max}+1} & \cdots & \tilde{\mathbf{w}}_D\end{bmatrix}$ containing the remaining eigenvectors after excluding $\tilde{\mathbf{w}}_{i_{\max}}$. We then decrement D by 1 and set $\mathbf{H} = \widehat{\mathbf{H}}_{\text{res}}$ and repeat the three steps to estimate the breathing rate of the next target.

IV. Experimental Setup and Data Collection

In this section, we describe the experimental setup and the experiments performed for the data collection.

A. Experimental Setup

Our experiments were carried out in the room shown in Fig. 2. We used two computer numerical control (CNC) machines each fitted with an aluminum foil covered reflection plate ($8\,\text{cm}$ x $12\,\text{cm}$) that can move back and forth to mimic human chest movement during respiration with a reproducable and fine-grained variable frequency. The openwifi FPGA board with the antennas was situated in the upper-right corner of the room. The two CNC machines were positioned in nine locations in the room, as shown in Fig. 2, providing different AoA and distances to the antennas. Specifically, the CNC machines were at distances of $0.5\,\text{m}$, $1.5\,\text{m}$, and $2.5\,\text{m}$ from the antennas and the AoAs were $0°$ (positions 1, 2, and 3), $45°$

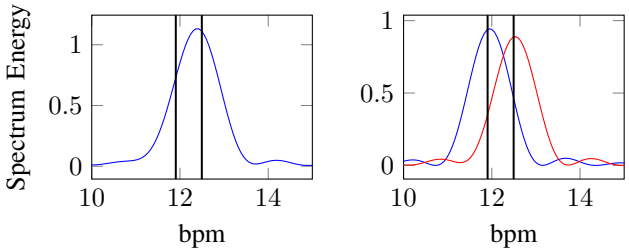

Fig. 3: Comparison between spectra calculated from the measured signal (left) and after separation with the proposed estimate-focus-delete method (right). The breathing rate of CNC 1 and CNC 2 are 11.91 bpm and 12.5 bpm, respectively. The vertical lines indicate these ground truth breathing rates.

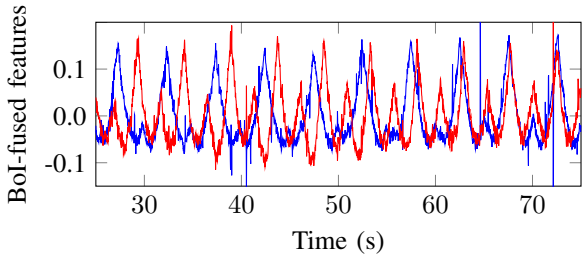

Fig. 4: BoI-fused features matching Fig. 3 spectrum.

(positions 4, 5, and 6), and 90° (positions 7, 8, and 9). While our setup does not emulate other potential human movements, this methodology is consistent with prevalent practices where human subjects remain stationary during data capture [8, 16, 20]. When movement is a factor, auxiliary systems that detect movement can be deployed to discard unreliable measurements during periods of significant motion [22]. Though we emulate only two breathing subjects, this number is realistic for home-monitoring situations like those in a bedroom.

The openwifi board was configured to operate in monitor mode, transmitting and receiving 40 packets per second. We used Wi-Fi channel 13, which has a carrier frequency of $f_c = 2472\,\mathrm{MHz}$ and we used a $20\,\mathrm{MHz}$ bandwidth. To increase the number of relevant paths, we enable two Tx antennas with cyclic delay diversity (CDD). This mode sends the same I/Q samples on both antennas with a $50\,\mathrm{ns}$ delay on the second Tx antenna. The corresponding spatially different paths appear as delayed paths in the CIR and are therefore partially distinguishable and can aid the breathing estimation and target separation process. From each Rx antenna, 3920 I/Q samples were captured for every injected Wi-Fi packet.

B. Data Collection

We consider two main data collection scenarios: multi-target sensing with CNC machines and validation with two human subjects. For the multi-target experiment, the CNC machines were programmed to oscillate with amplitudes of either $0.75\,\mathrm{cm}$ or $1\,\mathrm{cm}$ with a given frequency to simulate diaphragmatic excursions during quiet breathing [29]. Note that the CNC machines do not exactly follow these frequencies, due to a delay in changing direction when oscillating back and forth. Given that the CNC machines provide our ground-truth, we have calibrated their frequency based on the time required to complete a given number of cycles at each frequency. We operated two CNC machines simultaneously, with the first one running at a constant frequency of 11.91 bpm after calibration (the desired frequency is 12 bpm) and the second one cycling through a desired frequency range from 12 to 18 bpm in steps of 0.5 bpm. Since a main challenge for multi-target sensing is when breathing rates are very similar, we also include rates of 12.1, 12.2, 12.4, 12.6, and 12.8 bpm for the second machine for all experiments to cover these challenging cases. For clarity, any frequencies discussed henceforth will refer to the actual CNC frequency rates, not the desired ones. For all of these experiments, we collected I/Q samples for 1.5 minutes. Finally, for the validation with two human subjects, we obtained the reference respiration rate with Hexoskin smart garments [30].

V. Results

In this section, we present the results of our different experiments. First, we demonstrate how the proposed estimate-focus-delete method works on some example data. Then, we present results for the experiments with the CNC machines where we consider three main scenarios for multi-target sensing. Finally, we present the results for the validation with human breathing.

A. Estimate-Focus-Delete

In the left plot of Fig. 3, we show the average spectrum over the two antennas and delay bins when CNC 1 is at position 7 in Fig. 2 running at 11.91 bpm and CNC 2 is at position 1 running at 12.5 bpm. In this scenario, both CNC machines are at a distance of $0.5\,\mathrm{m}$. We observe that, even though there are two breathing rates present, these are not clearly distinguishable. Running our estimate-focus-delete method for two targets, we obtain the two extracted breathing signals shown in Fig. 4. The signal for the first target is in blue and for the second target in red. The corresponding spectra are shown in the right plot of Fig. 3, where one can clearly distinguish the two different breathing rates, even though they are very close.

B. Multi-Target Sensing

We now quantify the accuracy for multi-target sensing with the CNC machines. To this end, we consider three scenarios with different positions of the CNC machines in Fig. 2:

1) CNC 1 and 2 are at positions 1 and 5, respectively.
2) CNC 1 and 2 are at positions 2 and 9, respectively.
3) CNC 1 and 2 are at positions 1 and 2, respectively.

For each scenario, we estimate the breathing rates. For each frequency, we have several estimates as we use a sliding window of $50\,\mathrm{s}$ with a stride of $1\,\mathrm{s}$ over the data which has a length of $90\,\mathrm{s}$. The results are plotted in Fig. 5 over time

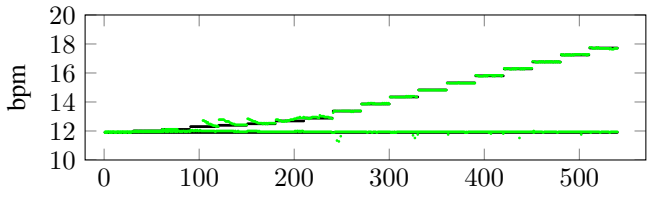

(a) Scenario 1: CNC 1 at position 1 (0.5 m distance and AoA 0°) and CNC 2 at position 5 (1.5 m distance and AoA 45°.

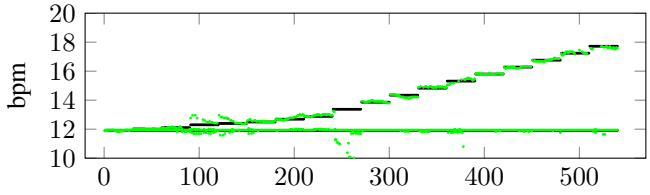

(b) Scenario 2: CNC 1 at position 2 (1.5 m distance and AoA 0°) and CNC 2 at position 9 (2.5 m distance and AoA 90°).

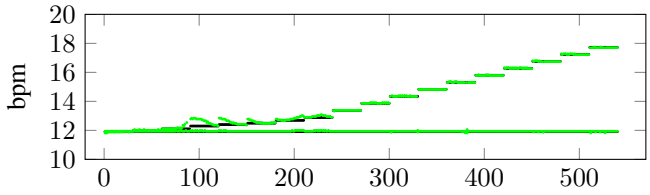

(c) Scenario 3: CNC 1 at position 1 (0.5 m distance and AoA 0°) and CNC 2 at position 2 (1.5 m distance and AoA 0°).

Fig. 5: Breathing rate estimates (bpm) for 3 scenarios shown in green, compared to ground truth in black (x-axis: estimate number from low to high frequency). Results are obtained for each frequency with a 50 s sliding window with a 1 s stride.

and Table I summarizes the average accuracy for different frequency-difference regions.

For scenario 1 in Fig. 5a we observe that we can accurately track the breathing rate for most frequencies, except for the frequencies slightly above the fixed frequency that CNC 1 runs at. For scenario 2 in Fig. 5b, we see that the estimates are in general are worse compared to scenario 1. This is because the distance of each CNC machine to the Rx antenna has increased by 1 m relative to scenario 2 which is expected to make the estimation harder. However, we also observe that the estimates generally remain close to the ground truth for most frequency differences. Finally, we have scenario 3 in Fig. 5b. In this scenario, the two CNC machines are positioned at the same AoA with a distance between them of 1 m. We observe that we can still obtain very accurate breathing rate estimates.

In all considered scenarios, we noticed an increased difficulty in tracking the frequency of CNC 2 when its frequency is marginally higher than that of CNC 1. This difficulty was particularly evident when the frequency difference ranged from approximately 0.2 to 0.8 bpm. For clarity, we zoom in to this frequency-difference (diff) region in Table I which shows three groups based on whether the ground truth frequency of CNC 2 falls within or outside this challenging range. Even within this challenging range, our estimation error generally did not exceed 1.0 bpm, barring scenario 1. Furthermore, our method demonstrates an average estimation error of less than 0.24 when the frequency of CNC 2 exceeds that of CNC 1 by more than 0.8 bpm, except for scenario 2. In scenario 2, the error increases to approximately 1.22 bpm due to the larger distance to the targets. We note that while our method struggles when the breathing rates are very close (respiration difference between targets is around 0.2 to 0.8 bpm), it is also not common to compare breathing rates as close as we do here. For instance, in [25], human subjects use metronomes to control their breathing at 15, 16.5, 18, 19.5, 21, 22.5, and 24 bpm which represents a step-size of 1.5 bpm.

TABLE I: Mean estimation error in bpm for the three scenarios. We divide the results into three groups to illustrate the critical region of very small frequency differences of the two targets.

	diff < 0.2	$0.2 \leq$ diff < 0.8	diff ≥ 0.8
Scenario 1	0.05	2.74	0.24
Scenario 2	0.07	0.94	1.22
Scenario 3	0.06	0.61	0.15

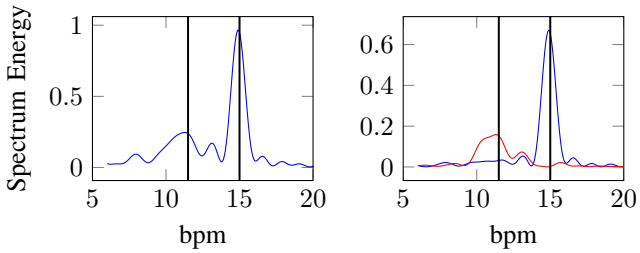

Fig. 6: Comparison between spectra calculated from the measured signal (left) and after separation with the proposed estimate-focus-delete method (right). The breathing rate of human subject 1 is 11.5 bpm and subject 2 is 15.0 bpm.

Finally, we emphasize that these results were achieved using only the passive cancellation from antenna separation. We thus demonstrate that this setup can work for sensing at a distance of a few meters without active cancellation, which significantly simplifies our monostatic sensing hardware.

C. Validation with Human Breathing

Finally, to validate our method in a real-world scenario, we also collected and analyzed human breathing data. The first person is sitting at position 2 in Fig. 2 with a ground-truth breathing rate of 11.5 bpm and the second person is sitting at position position 8 in Fig. 2 with a breathing rate of 15 bpm. Similar to the CNC machine experiments, we plot in Fig. 6 the spectra of the average over the two antennas and two used delay

bins (left) and of the separated breathing signals (right). For this experiment, both breathing rates are clearly visible, even without our estimation method and we also obtain the same breathing rate estimates of 11.28 bpm and 14.88 bpm with and without separation (by detecting the two largest peaks).

VI. Conclusion

In this paper, we presented the use of the open-source openwifi platform for monostatic multi-antenna Wi-Fi sensing. The testbed demonstrated a high degree of reliability and precision in the simultaneous estimation of the breathing rates of two targets, even in challenging scenarios. Moreover, our results suggest that self-interference cancellation, often a complex aspect in similar systems, is not necessary for close-range breathing rate sensing in our setup. While our measurements with CNC-machine based dummy targets and with two human subjects indicate that the setup can be used in practice for monostatic Wi-Fi sensing, we also recognize that more dynamic scenarios and more complex environments as well as comparison to bi-static platforms require further evaluation.

Acknowledgment

This research has been kindly supported by the Swiss National Science Foundation under Grant-ID 182621.

References

[1] S. S. Gambhir, T. J. Ge, O. Vermesh, and R. Spitler, "Toward achieving precision health," *Science Translational Medicine*, vol. 10, no. 430, p. eaao3612, 2018.

[2] P. C. Hallal, L. B. Andersen, F. C. Bull, R. Guthold, W. Haskell, and U. Ekelund, "Global physical activity levels: Surveillance progress, pitfalls, and prospects," *The Lancet*, vol. 380, no. 9838, pp. 247–257, 2012.

[3] S. G. Trost and M. O'Neil, "Clinical use of objective measures of physical activity," *British Journal of Sports Medicine*, vol. 48, no. 3, pp. 178–181, 2014.

[4] Y. Khan, A. E. Ostfeld, C. M. Lochner, A. Pierre, and A. C. Arias, "Monitoring of vital signs with flexible and wearable medical devices," *Advanced materials*, vol. 28, no. 22, pp. 4373–4395, 2016.

[5] S. A. Shah and F. Fioranelli, "RF sensing technologies for assisted daily living in healthcare: A comprehensive review," *IEEE Aerospace and Electronic Systems Magazine*, vol. 34, no. 11, pp. 26–44, 2019.

[6] Y. Hu, F. Zhang, C. Wu, B. Wang, and K. J. Ray Liu, "A WiFi-based passive fall detection system," in *ICASSP 2020 - 2020 IEEE International Conference on Acoustics, Speech and Signal Processing (ICASSP)*. IEEE, May 2020, pp. 1723–1727.

[7] F. Meneghello, D. Garlisi, N. D. Fabbro, I. Tinnirello, and M. Rossi, "Environment and person independent activity recognition with a commodity IEEE 802.11ac access point," *arXiv:2103.09924 [cs, eess]*, Mar. 2021.

[8] Q. Gao, J. Tong, J. Wang, Z. Ran, and M. Pan, "Device-free multi-person respiration monitoring using WiFi," *IEEE Transactions on Vehicular Technology*, vol. 69, no. 11, pp. 14 083–14 087, Nov. 2020.

[9] D. Halperin, W. Hu, A. Sheth, and D. Wetherall, "Tool release: Gathering 802.11n traces with channel state information," *ACM SIGCOMM Computer Communication Review*, vol. 41, no. 1, p. 53, Jan. 2011.

[10] Y. Xie, Z. Li, and M. Li, "Precise power delay profiling with commodity WiFi," in *Proceedings of the 21st Annual International Conference on Mobile Computing and Networking*, ser. MobiCom '15. ACM, 2015, p. 53–64.

[11] F. Gringoli, M. Schulz, J. Link, and M. Hollick, "Free your CSI: A channel state information extraction platform for modern Wi-Fi chipsets," in *Proceedings of the 13th International Workshop on Wireless Network Testbeds, Experimental Evaluation & Characterization - WiNTECH '19*. ACM Press, 2019.

[12] M. Atif, S. Muralidharan, H. Ko, and B. Yoo, "Wi-ESP—A tool for CSI-based device-free Wi-Fi sensing (DFWS)," *Journal of Computational Design and Engineering*, vol. 7, no. 5, pp. 644–656, Oct. 2020.

[13] Z. Jiang, T. H. Luan, X. Ren, D. Lv, H. Hao, J. Wang, K. Zhao, W. Xi, Y. Xu, and R. Li, "Eliminating the barriers: Demystifying Wi-Fi baseband design and introducing the PicoScenes Wi-Fi sensing platform," *arXiv:2010.10233 [cs]*, Mar. 2021.

[14] F. Gringoli, M. Cominelli, A. Blanco, and J. Widmer, "AX-CSI: Enabling CSI extraction on commercial 802.11ax Wi-Fi platforms," in *Proceedings of the 15th ACM Workshop on Wireless Network Testbeds, Experimental Evaluation & CHaracterization*. ACM, Jan. 2022, pp. 46–53.

[15] A. Liu, Z. Huang, M. Li, Y. Wan, W. Li, T. X. Han, C. Liu, R. Du, D. T. K. Pin, J. Lu, Y. Shen, F. Colone, and K. Chetty, "A survey on fundamental limits of integrated sensing and communication," Apr. 2021.

[16] Y. Zeng, D. Wu, J. Xiong, E. Yi, R. Gao, and D. Zhang, "FarSense: Pushing the range limit of WiFi-based respiration sensing with CSI ratio of two antennas," *Proceedings of the ACM on Interactive, Mobile, Wearable and Ubiquitous Technologies*, vol. 3, no. 3, pp. 1–26, Sep. 2019.

[17] M. Duarte and A. Sabharwal, "Full-duplex wireless communications using off-the-shelf radios: Feasibility and first results," in *2010 Conference Record of the Forty Fourth Asilomar Conference on Signals, Systems and Computers*. IEEE, Nov. 2010, pp. 1558–1562.

[18] X. Jiao, M. Mehari, W. Liu, M. Aslam, and I. Moerman, "Openwifi CSI fuzzer for authorized sensing and covert channels," in *Proceedings of the 14th ACM Conference on Security and Privacy in Wireless and Mobile Networks*. ACM, Jun. 2021, pp. 377–379.

[19] X. Jiao, W. Liu, M. Mehari, M. Aslam, and I. Moerman, "Openwifi: A free and open-source IEEE802.11 SDR implementation on SoC," in *2020 IEEE 91st Vehicular Technology Conference (VTC2020-Spring)*. IEEE, May 2020, pp. 1–2.

[20] X. Wang, C. Yang, and S. Mao, "PhaseBeat: Exploiting CSI phase data for vital sign monitoring with commodity WiFi devices," in *2017 IEEE 37th International Conference on Distributed Computing Systems (ICDCS)*. IEEE, Jun. 2017, pp. 1230–1239.

[21] J. Liu, Y. Chen, Y. Wang, X. Chen, J. Cheng, and J. Yang, "Monitoring vital signs and postures during sleep using WiFi signals," *IEEE Internet of Things Journal*, vol. 5, no. 3, pp. 2071–2084, Jun. 2018.

[22] Y. Zeng, D. Wu, J. Xiong, J. Liu, Z. Liu, and D. Zhang, "MultiSense: Enabling multi-person respiration sensing with commodity WiFi," *Proceedings of the ACM on Interactive, Mobile, Wearable and Ubiquitous Technologies*, vol. 4, no. 3, pp. 1–29, Sep. 2020.

[23] K. E. Barrett, S. M. Barman, S. Boitano, and H. L. Brooks, *Ganong's Review of Medical Physiology, 23e*. New York, NY: McGraw-Hill Medical, 2010.

[24] S. Li, A. T. Kristensen, A. Burg, and A. Balatsoukas-Stimming, "ComplexBeat: Breathing rate estimation from complex CSI," in *2021 IEEE Workshop on Signal Processing Systems (SiPS)*. IEEE, 2021, pp. 217–222.

[25] C. Chen, Y. Han, Y. Chen, and K. J. R. Liu, "Multi-person breathing rate estimation using time-reversal on WiFi platforms," in *2016 IEEE Global Conference on Signal and Information Processing (GlobalSIP)*. IEEE, Dec. 2016, pp. 1059–1063.

[26] X. Jiao, W. Liu, M. Mehari, H. Thijs, and A. Muhammad. (2023) open-source ieee802.11/wi-fi baseband chip/fpga design. [Online]. Available: https://github.com/open-sdr

[27] S. Li, A. Balatsoukas-Stimming, and A. Burg, "Band-of-interest-based channel impulse response fusion for breathing rate estimation with UWB," 2023, publisher: arXiv.

[28] B. Ghojogh, F. Karray, and M. Crowley, "Eigenvalue and generalized eigenvalue problems: Tutorial," 2019, publisher: arXiv Version Number: 2.

[29] A. Boussuges, Y. Gole, and P. Blanc, "Diaphragmatic motion studied by M-mode ultrasonography," *Chest*, vol. 135, no. 2, pp. 391–400, Feb. 2009.

[30] Carre Technologies Inc (Hexoskin). (2023) Hexoskin smart shirts-cardiac, respiratory, sleep & activity metrics. Accessed on 14.07.2023. [Online]. Available: https://www.hexoskin.com/